Uniaxial tensile response and tensile constitutive model of ultra-high performance concrete containing coarse aggregate (CA-UHPC)

Shi, Z.; Su, Q.; Kavoura, F.; Veljkovic, M.

Important note
To cite this publication, please use the final published version (if applicable).
Please check the document version above.

Uniaxial tensile response and tensile constitutive model of ultra-high performance concrete containing coarse aggregate (CA-UHPC)

Zhanchong Shi [a,b], Qingtian Su [a,c,*], Florentia Kavoura [b], Milan Veljkovic [b]

[a] *Department of Bridge Engineering, Tongji University, Shanghai, 200092, China*
[b] *Department of Engineering Structures, Delft University of Technology, 2628CN, Delft, the Netherlands*
[c] *Shanghai Engineering Research Center of High Performance Composite Bridges, Shanghai, 200092, China*

A R T I C L E   I N F O

A B S T R A C T

To establish the tensile constitutive model of ultra-high performance concrete containing coarse aggregate (CA-UHPC), monotonic and cyclic uniaxial tensile tests for CA-UHPC with fiber volume fractions of 2.5% and 2.0% were conducted. Test results showed that CA-UHPC exhibits approximately linear stress-strain relation up to the tensile strength, and tensile softening response composed of the smeared- and localized-cracking stages, regardless of the tested fiber contents. Based on the monotonic test data, the tensile stress-crack opening model of CA-UHPC was established, and the model was further simplified into tri-linear relation. Based on the cyclic test results, tensile damage evolution laws according to the strain equivalence principle and the energy equivalence principle were developed, respectively. Finally, the proposed tensile constitutive model and the calibrated tensile damage evolution laws were demonstrated to effectively predict the mechanical response of CA-UHPC members under both monotonic tension and cyclic tension through numerical simulations.

1. Introduction

Ultra-high performance concrete (UHPC) is a cementitious composite material with exceptional mechanical properties (compressive strength greater than 120 MPa, sustained post-cracking tensile strength greater than 5 MPa, modulus of elasticity greater than 45 GPa), superior energy absorption capacity and enhanced durability compared with conventional concrete [1–3]. To achieve such excellent mechanical properties, the water-to-binder ratio is usually less than 0.25 [1] by adopting large dosage of superplasticizer, and the particle sizes are optimized based on the dense particle packing theory. Because of the weak mechanical properties and flaws induced by the interfacial transition zone (ITZ) between the coarse aggregate and paste [4], the coarse aggregate is excluded in the common UHPC. The special material composition leads to exceptional mechanical properties as well as high production costs and severe autogenous shrinkage for UHPC [5,6], while the two main disadvantages have limited the mass application of UHPC in civil engineering. To deal with the above defects of UHPC, several attempts [7–10] have been made to introduce coarse aggregates to partially replace reactive powders in UHPC, i.e., UHPC containing coarse aggregate (CA-UHPC).

The addition of coarse aggregates increases the interfacial transition

zone, which will deteriorate the tensile mechanical properties of CA-UHPC compared with UHPC without coarse aggregate. The excellent post-cracking tensile properties is one of the most significant advantages for UHPC. Though coarse aggregates are incorporated, it is critical to ensure the abundant tensile properties for CA-UHPC. Therefore, investigations on the tensile behavior of CA-UHPC are essential for the design practice of CA-UHPC structures. Pyo et al. [5] studied the effect of coarse aggregates types (dolomite and basalt) and steel fiber contents (varying from 0.5% to 2.0%) on the first-cracking tensile strength, tensile strength, tensile strain capacity and cracking pattern of CA-UHPC. It is revealed that adopting dolomite aggregate with a maximum particle size of 5 mm can achieve adequate tensile capabilities compared with the typical UHPC, and the usage of basalt aggregate is not helpful to improve the tensile properties. The combined effect of coarse aggregate contents (replacement volume of mortar of 0%, 15%, 25%, 35%) and steel fiber types on tensile behavior of CA-UHPC was experimentally investigated by Liu et al. [11]. The test results demonstrated that coarse aggregate can be successfully adopted in UHPC when the replacement level is within 25%. In addition, the strain-hardening response of CA-UHPC could be achieved by increasing the steel fiber volume fraction larger than 2.5%. Li et al. [12] reported that the optimal powder contents are 800 kg/m^3 and 700 kg/m^3 for CA-UHPC incorporating

Table 1
Material compositions of 1 m³ CA-UHPC with different fiber contents (unit: kg).

Number	Reactive powder	River sand	Basalt aggregate	Steel fibers		Superplasticizer	Water
				straight	hooked		
U-2.5%	1173	616	472	89	109	25.7	138
U-2.0%	1173	616	472	72	88	25.7	138
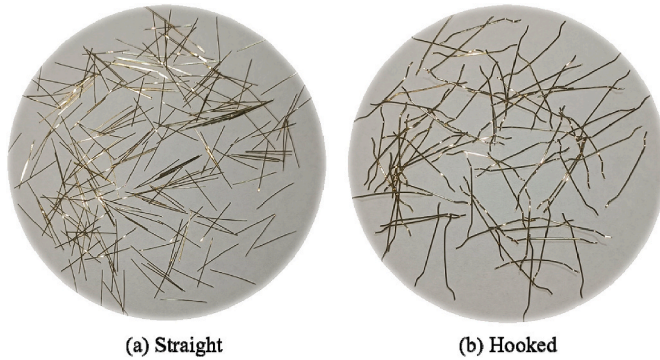
Fig. 1. Types of steel fibers: (a) straight, 13 mm × 0.2 mm; (b) hooked, 20 mm × 0.25 mm.

maximum basalt aggregate size of 8 mm and 16 mm, and longer steel fibers (compared with short steel fibers with length of 13 mm and diameter of 0.2 mm) are suggested in CA-UHPC considering the tensile strength. Wang et al. [13] reported that the flexural tensile strength of UHPC decreases 10.4% when the equal content of powder is replaced by 580 kg/m³ river sand and 600 kg/m³ basalt aggregate. In summary, existing studies on the tensile behavior of CA-UHPC mainly focused on the influence of coarse aggregate types, coarse aggregate contents, fiber types, and fiber contents.

However, research on the tensile constitutive model of CA-UHPC is in preliminary stages. With the increasing engineering application of CA-UHPC, such as bridge deck systems [14,15] and structural columns [6], an appropriate tensile constitutive model is critical to the theoretical and numerical analysis of CA-UHPC structures [16]. In addition, the concrete damaged-plasticity model (CDP) proposed by Lubliner et al. [17] is adopted in ABAQUS to conduct nonlinear finite element analysis and damage analysis of concrete structures. The tensile damage variable of CDP for normal concrete (NC) could adopt the tensile damage which is obtained through the cyclic uniaxial tensile test and is in the form of reduction of deformation modulus. This has been validated by Lee et al. [18]. Compared with NC without fibers, steel fibers play an important role to bridge cracks and transfer stresses in the tensile softening stage for CA-UHPC. Hence, whether the tensile damage variable obtained by the cyclic uniaxial tensile test could be directly used in CDP of ABAQUS for CA-UHPC also deserves investigation and discussion. Furthermore, no relevant cyclic uniaxial tensile test of CA-UHPC has been reported except for that of the typical UHPC without coarse aggregate [19–21].

To address these gaps, monotonic and cyclic uniaxial tensile tests for CA-UHPC with steel fiber volume fractions of 2.5% and 2.0% were conducted, respectively. The tensile stress-crack opening model and the tensile stress-strain model for CA-UHPC were developed. The tensile damage evolution laws based on the strain equivalence principle (SEP) and the energy equivalence principle (EEP) respectively were established and calibrated. The proposed tensile constitutive model and the calibrated tensile damage evolution laws were verified through the comparison of the load-displacement responses of test results and numerical simulations.
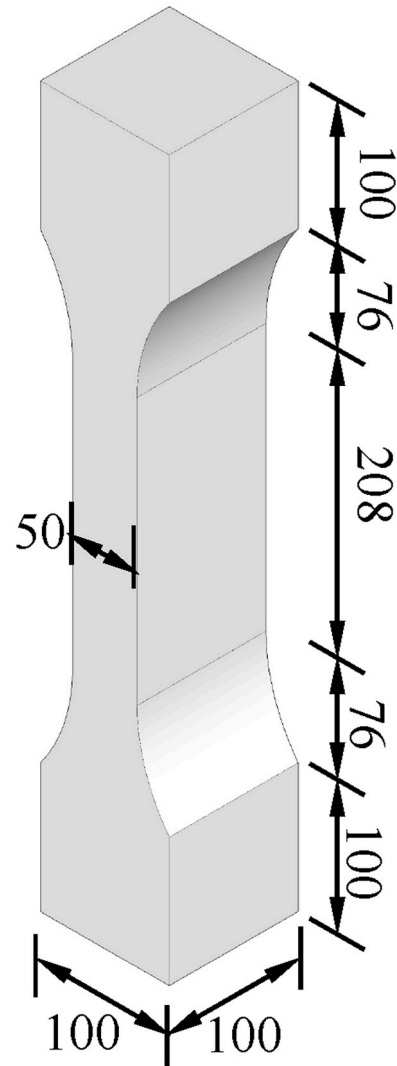
Fig. 2. Dog-bone shaped specimen (unit: mm).

2. Experimental program

2.1. Materials and specimen preparation

The CA-UHPC used was a commercial concrete, which was composed of reactive powder, river sand, basalt aggregate with a maximum particle size less than 8 mm, superplasticizer, water, and steel fibers. The material compositions of 1 m³ CA-UHPC with fiber volume fractions of 2.5% and 2% (marked as U-2.5% and U-2.0%, respectively) were listed in Table 1. As shown in Fig. 1, the steel fibers contained the straight fibers (length of 13 mm and diameter of 0.2 mm) and the hooked-end fibers (length of 20 mm and diameter of 0.25 mm), and the mass ratio of the straight fibers to the hooked-end fibers was 44:45. The modulus of elasticity and tensile strength of the two steel fibers were 200 GPa and 2850 MPa, respectively.

Regarding the mixing process of CA-UHPC, the dry ingredients, i.e.,

Table 2
Specimen number and loading method.

Specimen number	Loading method	Specimen number	Loading method
U-2.5%-SN-1	Monotonic	U-2.0%-SN-1	Monotonic
U-2.5%-SN-2		U-2.0%-SN-2	
U-2.5%-SN-3		U-2.0%-SN-3	
U-2.5%-SN-4	Cyclic	U-2.0%-SN-4	Cyclic
U-2.5%-SN-5		U-2.0%-SN-5	
U-2.5%-SN-6		U-2.0%-SN-6	

Fig. 4. Crack observation instrument.
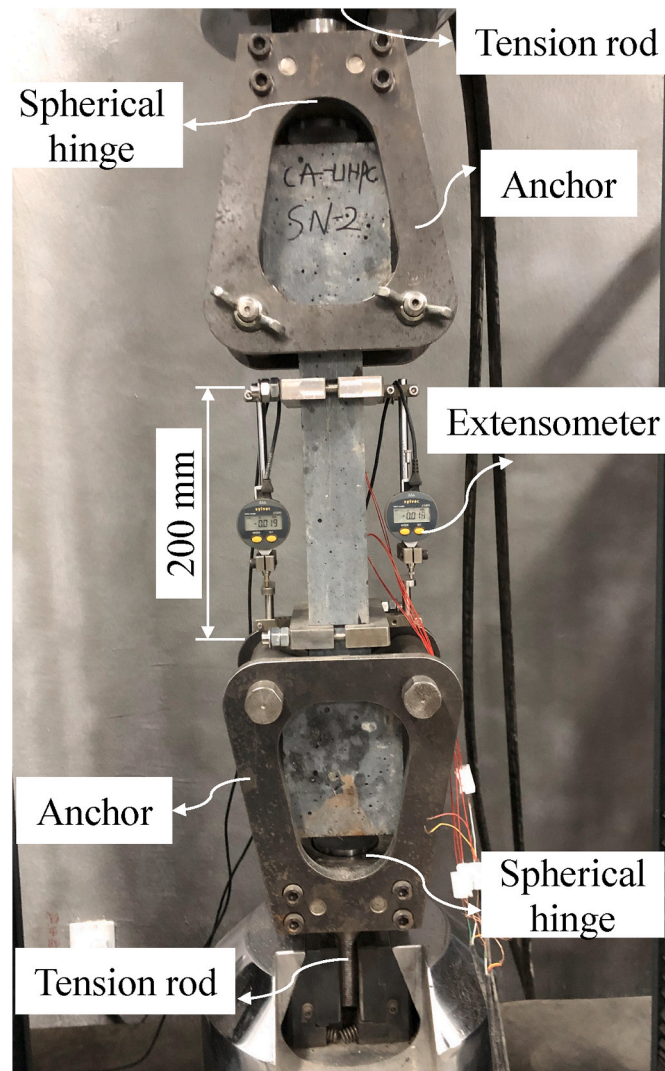

Fig. 5. Cyclic loading protocol.

Fig. 3. Uniaxial tensile test setup.

reactive powders, river sand and basalt aggregates, were initially mixed for 20 s to achieve uniform dispersion. Then superplasticizer and water were added, and the wet mixture was mixed for 4 min. Finally, the steel fibers were added gradually for 1 min, and the mixture was mixed for 3 min to achieve a homogeneous distribution of steel fibers. The fresh mixture was then cast into the plastic molds and vibrated on a vibrating table for 2–3 min. Then the specimens were covered with plastic film to prevent moisture loss. The specimens were demolded 24 h after casting and cured for 28 days under the standard curing condition, where the temperature and relative humidity were controlled at 20 °C and 95%, respectively.
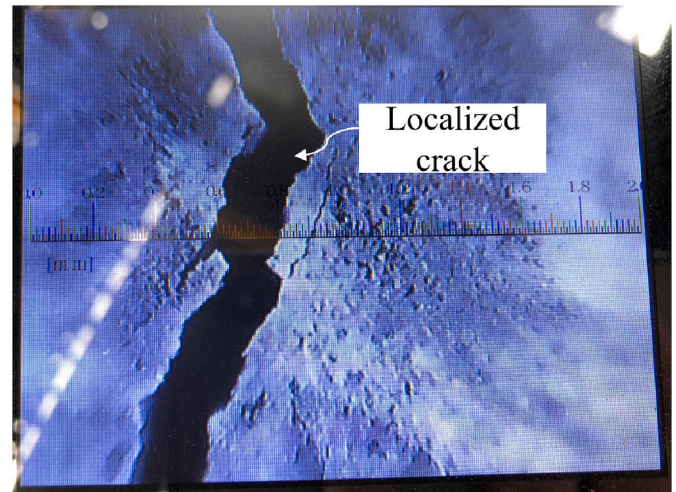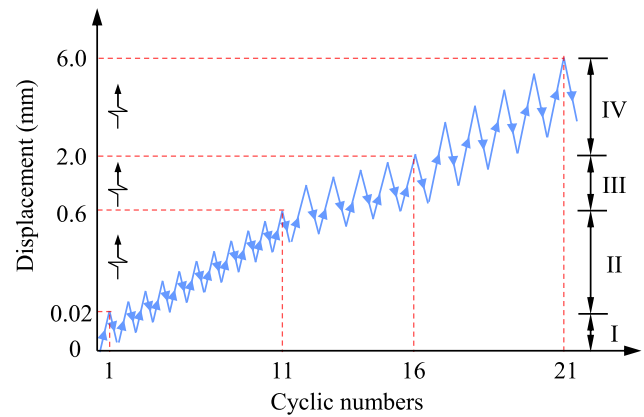
2.2. Test setup and loading protocols

A total of six dog-bone-shaped CA-UHPC specimens were casted for each fiber content. The specimen geometry is plotted in Fig. 2. The specimen number and the loading methods are listed in Table 2. The first three specimens SN-1 to SN-3 were tested under monotonic tensile loading, and the rest three specimens SN-4 to SN-6 were tested under cyclic tensile loading.

Fig. 3 shows the uniaxial tensile test setup. A servo-hydraulic testing machine was used to enforce direct tensile load to the specimen under displacement control. The axial elongation over a length of 200 mm was recorded by two extensometers attached to the specimen. Besides, the crack opening changes occurring within the gauge length were captured by a crack observation instrument with an accuracy of 0.01 mm, as shown in Fig. 4.

For the monotonic loading, the specimens were loaded under displacement control at a speed rate of 0.3 mm/min. Regarding the cyclic loading, the corresponding loading protocol is illustrated in Fig. 5. The displacement in Fig. 5 denoted the elongation within the gauge length of 200 mm. The loading procedure consisted of 21 loading-unloading cycles, and was divided into four phases. Phase I was performed to obtain the elastic modulus. Phase II, phase III, and phase IV induced tensile strain ranging from 0.0001 to 0.003, from 0.003 to 0.01, and from 0.01 to 0.03, respectively. The increments of displacement gradients for phase II, phase III, and phase IV were 0.058 mm, 0.28 mm, and 0.8 mm, respectively. The loading-unloading displacement rate was
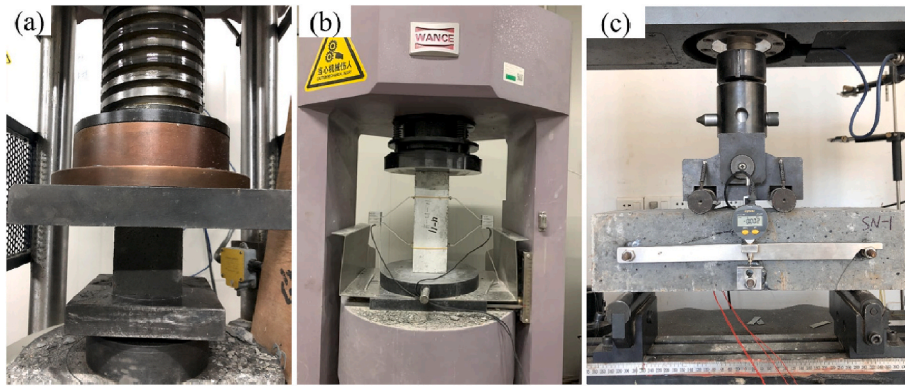
Fig. 6. Mechanical properties tests of CA-UHPC: (a) cubic compressive strength test; (b) elastic modulus and axial compressive strength tests; (c) four-point bending test.

Table 3
Basic mechanical properties of CA-UHPC with different fiber contents (unit: MPa).

Number	E_c	f_c	f_{cu}	$f_{cr,fl}$	$f_{ct,fl}$
U-2.5%	52000 ± 815	128 ± 10	141 ± 3	12.18 ± 0.19	23.65 ± 0.26
U-2.0%	48200 ± 1150	113 ± 5	126 ± 7	11.48 ± 0.63	18.35 ± 0.40

Notes: E_c, f_c, f_{cu}, $f_{cr,fl}$, $f_{ct,fl}$ denote elastic modulus, axial compressive strength, cubic compressive strength, first cracking strength under flexural tension and flexural strength, respectively.
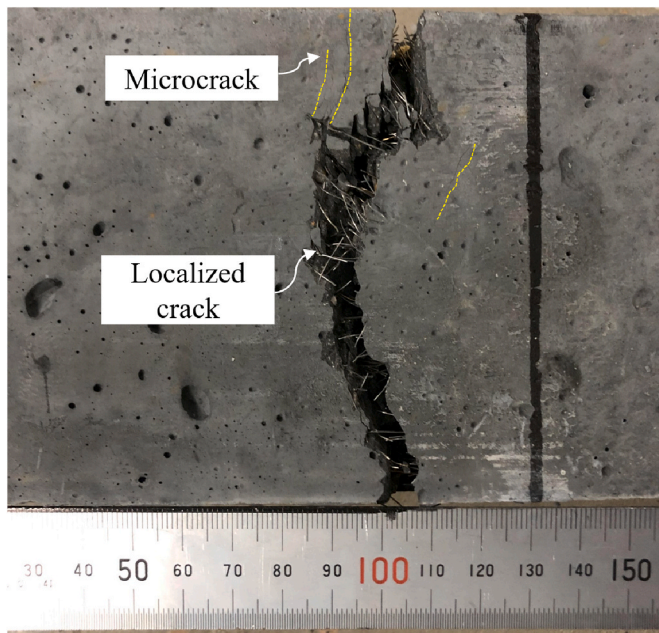

Fig. 7. The maximum crack opening (unit:mm).

kept constant at 0.5 mm/min.

2.3. Basic mechanical properties

Referring to Chinese Standard CECS13 [22], specimen sizes of 100 mm × 100 mm × 300 mm, 100 mm × 100 mm × 300 mm, 100 mm × 100 mm × 100 mm, and 100 mm × 100 mm × 400 mm, were used for obtaining the elastic modulus, axial compressive strength, cubic compressive strength, and flexural strength, respectively. The corresponding tests are plotted in Fig. 6. Each test had three identical specimens, and the related mean values and standard deviation of the basic mechanical properties (calculated according to Chinese Standard

Fig. 8. Fracture surfaces: (a) monotonic loading; (b) cyclic loading.

CECS13 [22])of CA-UHPC are summarized in Table 3.

3. Test results and analysis

3.1. Failure modes

The specimens tested under monotonic and cyclic tensile loading presented similar failure modes. It was observed that 2–3 microcracks with crack spacing approximately of 5–10 mm appeared within the gauge length when loaded to the peak load. Then localized crack formed after the peak load and the crack opening developed continuously. When the specimen was unable to bear the tensile load, the CA-UHPC matrix was fractured into two parts which were still connected by the partially pulled-out steel fibers, and the maximum crack opening could be obtained consequently. As plotted in Fig. 7, the maximum crack opening is equal to 6–7 mm which is close to half of the straight steel fiber length (13 mm).

The fractured specimens were forced to break into two pieces completely, and the fracture surfaces are shown in Fig. 8. It is clear that the fracture surface of the monotonic loading specimen is rough and is distributed with partially debonding steel fibers and coarse aggregates. While the matrix pulverization is scattered on the fracture surface for the cyclic loading specimen, and this could be interpreted by the fiber/
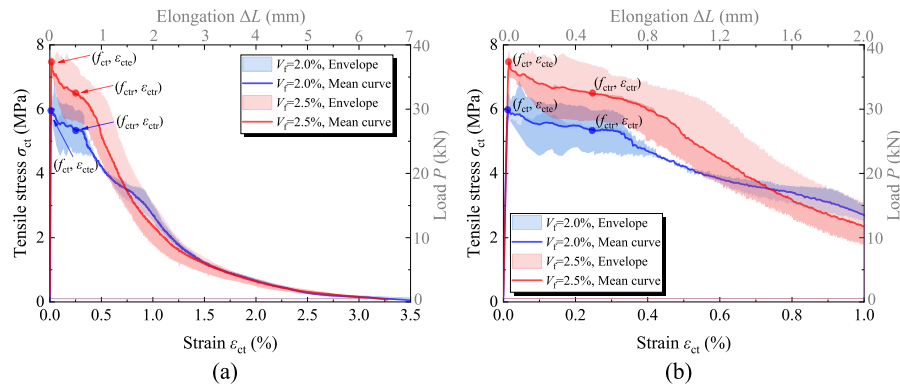
Fig. 9. Tensile stress-strain (load-elongation) curves of CA-UHPC under monotonic loading: (a) complete curve; (b) strain from 0 to 1.0%.
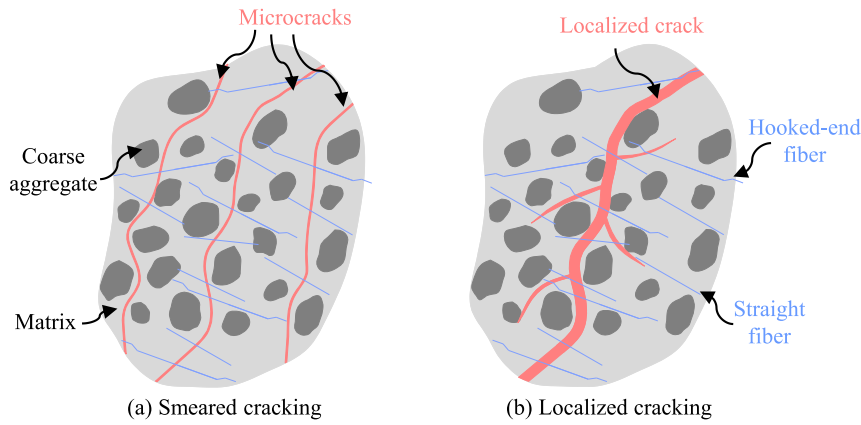

(a) Smeared cracking

(b) Localized cracking

Fig. 10. Cracking patterns.

matrix grinding and coarse aggregate/matrix grinding under cyclic loading.

3.2. Tensile stress-strain response

Fig. 9 shows the tensile stress-strain curves and load-elongation curves of CA-UHPC. In general, the two tensile stress-strain mean curves exhibit a similar response, which is featured by the approximately linear stress-strain relation up to the peak stress, i.e., the tensile strength f_{ct}, and the post-peak tensile softening response. The French code [3] classifies the UHPC material into three types, strain-hardening, low strain-hardening and strain-softening, according to the post-elastic-limit tensile stress-strain response. Based on this criterion, the tested CA-UHPC is classified as the strain-softening type consequently. The tensile strain ε_{cte} corresponding to the tensile strength f_{ct} is the elastic limit tensile strain, and the tensile elastic modulus E_{ct} could be obtained by dividing the tensile strength by the elastic limit tensile strain.

The post-peak strain-softening response could be decomposed into the first descending branch featured by the smeared cracking, and the second descending branch featured by the localized cracking. The two descending branches are distinguished by the residual strength point $(f_{ctr}, \varepsilon_{ctr})$, where f_{ctr} is named as the residual tensile strength, and ε_{ctr} is the related tensile strain and is taken as 0.0025. Fig. 10 illustrates the smeared-cracking and localized-cracking patterns. At the smeared-cracking stage, 2–3 microcracks may initiate at the ITZ between coarse aggregate and matrix as this zone is the weakest to sustain tension. With the increase of tensile strain, one of the microcracks becomes the main crack due to strain localization, thus the smeared-cracking stage is transformed into the localized-cracking stage. This also could

Table 4
The characteristic parameters of the tensile stress-strain curve for CA-UHPC with a fiber volume fraction of 2.5%.

Number	f_{ct} (MPa)	ε_{cte} ($\times 10^{-6}$)	E_{ct} (MPa)	f_{ctr} (MPa)	ε_{ctr} ($\times 10^{-6}$)
U-2.5%-SN-1	7.90	143	55443	7.36	2500
U-2.5%-SN-2	7.83	183	42892	5.64	2500
U-2.5%-SN-3	7.75	148	52559	6.40	2500
Mean	7.83	158	50298	6.47	2500
Cov	1%	13%	13%	13%	0

Table 5
The characteristic parameters of the tensile stress-strain curve for CA-UHPC with a fiber volume fraction of 2.0%.

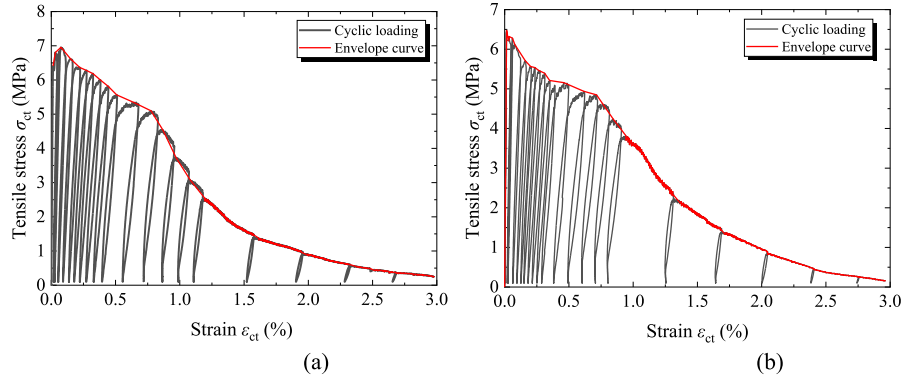| Number	f_{ct} (MPa)	ε_{cte} ($\times 10^{-6}$)	E_{ct} (MPa)	f_{ctr} (MPa)	ε_{ctr} ($\times 10^{-6}$)
U-2.0%-SN-1	5.74	117	48870	5.45	2500
U-2.0%-SN-2	5.79	120	48255	4.70	2500
U-2.0%-SN-3	6.52	125	52171	5.96	2500
Mean	6.03	121	49765	5.37	2500
Cov	7%	3%	4%	12%	0

Fig. 11. Typical tensile stress-strain curves of CA-UHPC under cyclic loading: (a) $V_f = 2.5\%$; (b) $V_f = 2.0\%$.
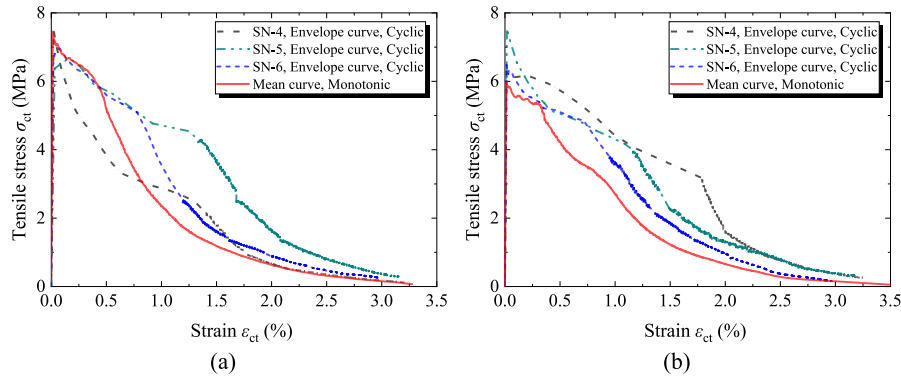

Fig. 12. Comparison of the tensile stress-strain curves of CA-UHPC under monotonic loading and cyclic loading: (a) $V_f = 2.5\%$; (b) $V_f = 2.0\%$.

be interpreted by the energy balance approach [23], localized crack develops when the amount of energy absorbed in widening one distinct crack opening is less than the energy absorbed in initiating new cracks.

The characteristic parameters of the tensile stress-strain curve for CA-UHPC with fiber volume fractions of 2.5% and 2.0% are summarized in Table 4 and Table 5, respectively. It is evident that the mean value of the tensile elastic modulus E_{ct} is almost equal to the compressive elastic modulus E_c listed in Table 3. The residual tensile strength f_{ctr} is approximately 10%–20% decrease of the tensile strength f_{ct}. Besides, the tensile strength and the elastic tensile strain of CA-UHPC with a fiber content of 2.5% are 29% and 30%, respectively, higher than the counterparts of 2.0%.

Fig. 11 shows the typical tensile stress-strain curves of CA-UHPC under cyclic loading, and Fig. 12 illustrates the comparison of the cyclic envelope curve and the monotonic mean curve. As shown, the monotonic mean curve is consistent with the cyclic envelope curve to some extent, indicating that the monotonic tensile stress-strain curve could be adopted to predict the cyclic envelope curve. And this has been validated in previous research for the typical UHPC without coarse aggregate [19–21].

3.3. Tensile damage evolution law

The matrix fracture and the steel fibers/matrix deboning develop at the tensile softening stage of CA-UHPC. This phenomenon is a symbol of continuous damage according to the continuum damage mechanics, and the damage state can be quantified by the damage variable D as shown in Eq. (1).

$$D = \frac{S_d}{S} = \frac{S - \overline{S}}{S} \tag{1}$$

where S is the overall section area, S_d is the damaged area, and $\overline{S}$ is the remaining effective area.

The stress resisted by the remaining effective area $\overline{\sigma}$ is called the effective stress $\overline{S}$. The relation between the effective stress $\overline{\sigma}$ and the stress σ which is sustained by the overall section area S could be derived,

$$\overline{\sigma} = \frac{S}{S - S_d} \sigma = \frac{\sigma}{1 - D} \tag{2}$$

In the next procedure, the Lemaitre's strain equivalence principle (SEP) [24] and Sidoroff's energy equivalence principle (EEP) [25] are introduced respectively to derive the formula of damage variable D.

3.3.1. Strain equivalence principle (SEP)

The SEP [24] assumes that the damaged area under the action of stress σ is identical to the overall section area under the action of the effective stress, as shown in Eq. (3).

$$\frac{\overline{\sigma}}{E_{c0}} = \frac{\sigma}{E_{cd}} \tag{3}$$

where E_{c0} is the elastic modulus of the non-damaged material, E_{cd} is the elastic modulus of the damaged material.

According to Eq. (2) and Eq. (3), the damage variable D is derived as following,

$$D = 1 - \frac{E_{cd}}{E_{c0}} \tag{4}$$

Based on the SEP, the tensile damage of CA-UHPC under cyclic loading is defined as the degradation of deformation modulus during the loading-unloading process. The tensile damage variable $D_{t,SEP}$ of CA-UHPC under cyclic loading is derived as,

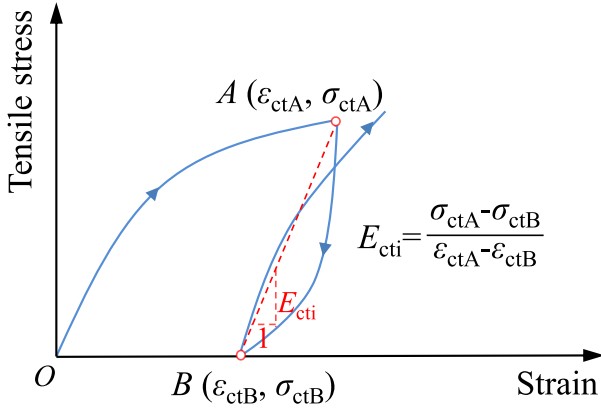$$D_{t,SEP} = 1 - \frac{E_{cti}}{E_{ct}} \tag{5}$$

6

Fig. 13. Calculation method of tensile deformation modulus under cyclic loading.

where E_{ct} is the tensile elastic modulus which is obtained in the first cycle, E_{cti} is the tensile deformation modulus in the rest cycles and the calculation method of E_{cti} is illustrated in Fig. 13.

The evolution of tensile damage variable of CA-UHPC based on the SEP is shown in Fig. 14. The tensile damage variable-strain relation is fitted in the form of exponential function as shown in Eq. (6), and the fitted parameters are listed in Table 6.

$$D_t = 1 - a_1 e^{-a_2 \varepsilon_{ct}} - a_3 e^{-a_4 \varepsilon_{ct}} \tag{6}$$

As illustrated in Fig. 14, the tensile damage variable develops rapidly when strain ranges from 0 to 0.0006 for CA-UHPC with the two fiber contents. This stage is mainly characterized by the microcracks occurring at the coarse aggregate/matrix interfaces. Then the evolution of the tensile damage variable slows down as the steel fibers come to bridge cracks and transfer stresses across the cracks. The comparison of the characterized tensile damage variable for CA-UHPC with the two fiber contents is listed in Table 7. As shown, the tensile damage difference of the two fiber contents is within 15% when the tensile strain is less than 0.001. While the tensile damage difference between the two fiber contents could be neglected when the tensile strain is larger than 0.002, where the localized cracking develops and the fiber-matrix debonding plays an important role. In general, the tensile damage of the CA-UHPC with a fiber volume fraction of 2.0% is close to that of a fiber volume fraction of 2.5%. This could be explained by the small difference in fiber contents.

3.3.2. Energy equivalence principle (EEP)

According to the EEP [25], the elastic residual energy produced by the damaged material is in the same form of that produced by the non-damaged material as long as the stress is substituted by the effective stress or the elastic modulus is replaced by the damaged elastic modulus.

The elastic residual energy of the non-damaged material and the equivalent elastic residual energy of the damaged material are shown below, respectively.

$$W_0^e = \frac{\sigma^2}{2E_0} \tag{7}$$

$$W_d^e = \frac{\overline{\sigma}^2}{2E_{c0}} = \frac{\sigma^2}{2E_{cd}} \tag{8}$$

The damage variable is derived by substituting Eq. (2) into Eq. (8).

$$D = 1 - \sqrt{\frac{E_{cd}}{E_{c0}}} \tag{9}$$

Based on the EEP, the tensile damage variable $D_{t,EEP}$ of CA-UHPC under cyclic loading is obtained, as expressed in Eq. (10).

$$D_{t,EEP} = 1 - \sqrt{\frac{E_{cti}}{E_{ct}}} \tag{10}$$

The evolution of tensile damage variable of CA-UHPC based on the EEP is shown in Fig. 15. The tensile damage variable-strain relation is also fitted according to Eq. (6), and the fitted parameters are

Table 6
Fitted parameters of tensile damage evolution law.

Damage Variable	Number	a_1	a_2	a_3	a_4
$D_{t,SEP}$	U-2.5%	0.168	104.185	1.153	3625.543
	U-2.0%	0.147	74.647	1.096	2582.846
$D_{t,EEP}$	U-2.5%	0.760	2220.125	0.369	38.940
	U-2.0%	0.752	1745.563	0.361	30.262

Table 7
Comparison of the characterized tensile damage variable for two fiber contents.

Strain	Tensile damage variable $D_{t,SEP}$			Tensile damage variable $D_{t,EEP}$		
	U-2.5%	U-2.0%	Difference	U-2.5%	U-2.0%	Difference
0.0005	0.653	0.557	14.7%	0.387	0.330	14.6%
0.001	0.818	0.781	4.6%	0.562	0.519	7.7%
0.002	0.863	0.867	−0.4%	0.649	0.637	1.8%
0.003	0.877	0.882	−0.5%	0.670	0.667	0.5%
0.01	0.941	0.930	1.1%	0.749	0.733	2.1%
0.02	0.979	0.967	1.2%	0.830	0.803	3.3%

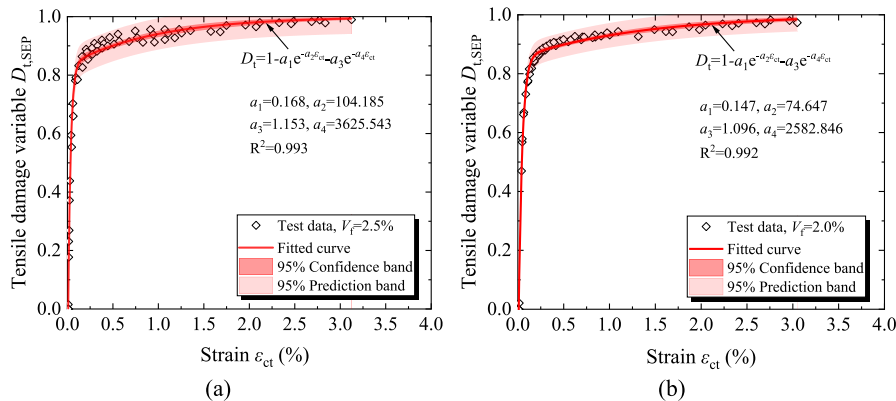Notes: Difference=$(D_{t,U-2.5\%} - D_{t,U-2.0\%})/D_{t,U-2.5\%}$.

Fig. 14. Evolution of the SEP-based tensile damage variable of CA-UHPC: (a) V_f = 2.5%; (b) V_f = 2.0%.
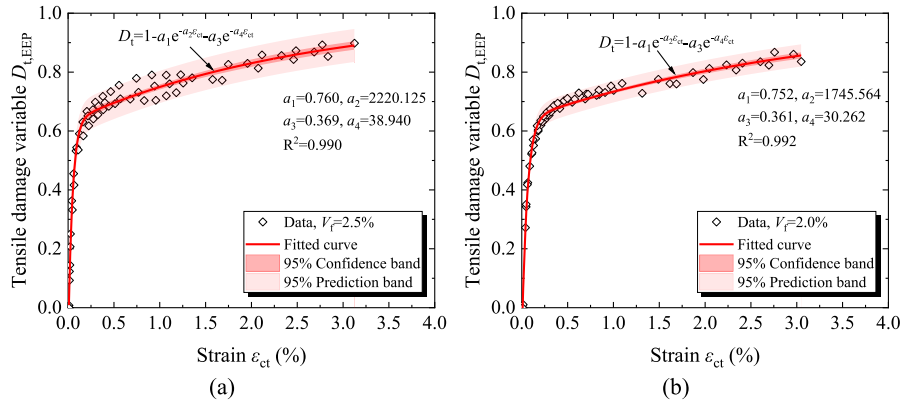
Fig. 15. Evolution of the EEP-based tensile damage variable of CA-UHPC: (a) $V_f = 2.5\%$; (b) $V_f = 2.0\%$.
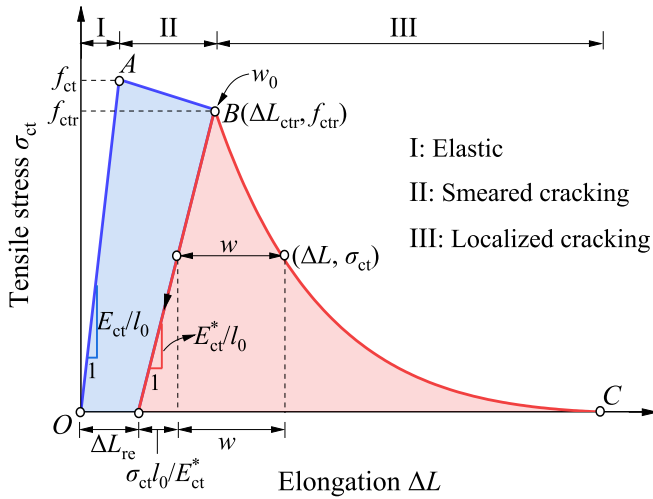

Fig. 16. Tensile stress-elongation response.

summarized in Table 6. The comparison of the EEP-based characterized tensile damage variable for CA-UHPC with the two fiber contents is listed in Table 7. As shown, the tensile damage variable $D_{t,EEP}$ of the CA-UHPC with a fiber volume fraction of 2.5% exhibits slightly larger than that of a fiber volume fraction of 2.0%, and the discrepancy is negligible.

4. Tensile constitutive model

4.1. Tensile stress-crack opening model

Based on the aforementioned test results, the tensile stress-elongation response of CA-UHPC is composed of three stages, the elastic stage, the linear softening stage featured by the smeared cracking, and the exponential softening stage featured by the localized cracking, as illustrated in Fig. 16. The tensile constitutive model of CA-UHPC could be described by the tensile stress-strain relation at the elastic stage and the tensile stress-crack opening relation at the softening stage, as shown in Fig. 17. The tensile stress-strain relation, as well as the tensile stress-crack opening relation, could be converted from the tensile stress-elongation relation.

The tensile stress-strain relation at the elastic stage,

$$\sigma_{ct} = \frac{f_{ct}}{\varepsilon_{cte}} \cdot \varepsilon_{ct} \quad \text{or} \quad E_{ct} \cdot \varepsilon_{ct} \quad 0 < \varepsilon_{ct} \leq \varepsilon_{cte} \tag{11}$$

where f_{ct} is the tensile strength, ε_{cte} is the elastic limit tensile strain, E_{ct} is the tensile elastic modulus, ε_{ct} is tensile strain, the values of these parameters are listed in Tables 4 and 5.

The crack opening w_0 at point B (see Fig. 16) is captured by a crack observation instrument during the monotonic loading, and the measured crack opening is approximately 0.2–0.4 mm. The crack opening w_0 is taken as 0.3 mm here for CA-UHPC with fiber volume fractions of 2.5% and 2.0%. The tensile stress-crack opening relation at the linear softening stage is described as,

$$\sigma_{ct} = f_{ct} + \frac{f_{ctr} - f_{ct}}{w_0} \cdot w \quad 0 < w \leq w_0 \tag{12}$$

where f_{ctr} is the residual tensile strength as listed in Tables 4 and 5, w_0 is the crack opening corresponding to the residual tensile f_{ctr} and is 0.3 mm, w is the crack opening.

The elongation at the exponential softening stage consists of the crack opening increment of the localized macrocrack and retraction of uncracked region within the gauge length. The geometric relation between the elongation and the crack opening is plotted in Fig. 16. The tensile stress-crack opening model at the exponential softening stage is derived as,
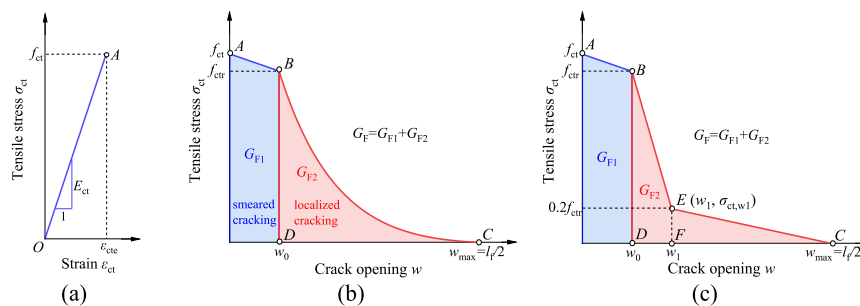

Fig. 17. Tensile stress-crack opening model: (a) elastic stage; (b) linear-exponential softening model; (c) simplified tri-linear softening model.
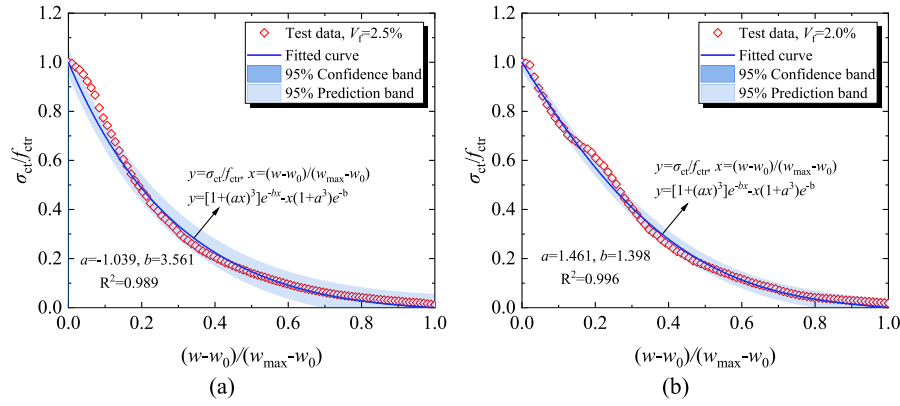
Fig. 18. The fitted tensile stress-crack opening relation at the exponential softening stage: (a) $V_f = 2.5\%$; (b) $V_f = 2.0\%$.

Table 8
Fracture energy of CA-UHPC and cracking opening at inflection point.

Number	G_{F1} (N/mm)	G_{F2} (N/mm)	G_F (N/mm)	w_1 (mm)
U-2.5%	2.15	10.21	12.36	2.22
U-2.0%	1.70	9.71	11.41	2.54

$$w = w_0 + \left(\Delta L - \Delta L_{re} - \frac{\sigma_{ct}}{E_{ct}^*} l_0 \right) \tag{13}$$

$$\Delta L_{re} = \Delta L_{ctr} - \frac{f_{ctr}}{E_{ct}^*} l_0 \tag{14}$$

where ΔL is elongation within the gauge length, ΔL_{re} is the irreversible elongation when unloading at the point B and is expressed in Eq. (14), l_0 is the gauge length. E_{ct}^* is the unloading deformation modulus at point B and could be obtained in the cyclic loading test. E_{ct}^* are 6519 MPa and 6157 MPa for CA-UHPC with fiber volume fractions of 2.5% and 2.0%, respectively. ΔL_{ctr} is the elongation at point B and is taken as 0.5 mm.

Based on the test data and the above relations, the tensile stress-crack opening relation at the exponential softening stage is fitted in the form of exponential function proposed by Hordijk [26], as expressed in Eq. (15).

$$\frac{\sigma_{ct}}{f_{ctr}} = \left[1 + \left(a \frac{w - w_0}{w_{max} - w_0} \right)^3 \right] e^{-b \frac{w - w_0}{w_{max} - w_0}} - \frac{w - w_0}{w_{max} - w_0} (1 + a^3) e^{-b} \quad w_0 < w$$

$$\leq w_{max} \tag{15}$$

where w_{max} is the maximum crack opening and is taken as 6.5 mm which is half of the straight steel fiber length $l_f/2$ ($l_f = 13$ mm), a and b are unknown parameters to be fitted.

Fig. 18 shows the fitted results which exhibit high reliability since the R-square is close to 0.99. The fitted a and b are -1.039 and 3.561 for CA-UHPC with a fiber volume fraction of 2.5%, and are 1.461 and 1.398 for CA-UHPC with a fiber volume fraction of 2.0% respectively.

According to the fictitious crack model (FCM) proposed by Hillerborg [23], the fracture energy expressed in Eq. (16) of concrete under tension denotes the amount of energy absorbed per unit crack area in widening crack opening from zero to or beyond w_{max}. As shown in Fig. 17(b) and expressed in Eq. (17), the fracture energy G_F of CA-UHPC herein is decomposed into G_{F1} for the smeared cracking and G_{F2} for the localized cracking. The FCM-based fracture energy of CA-UHPC is listed in Table 8.

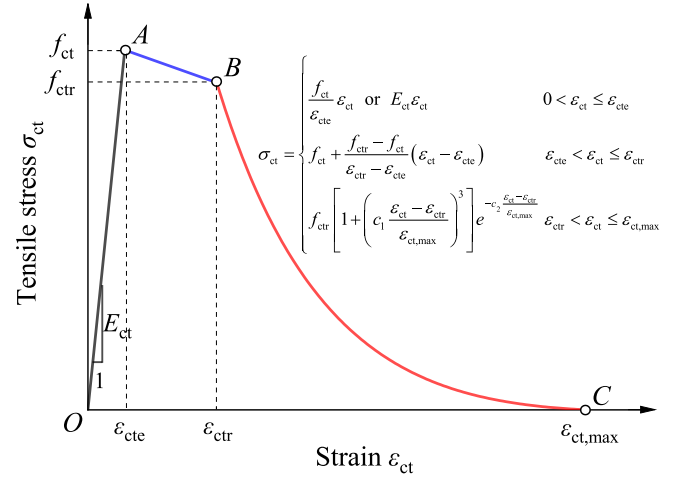$$G_F = \int_0^{w_{max}} \sigma_{ct}(w) d_w \tag{16}$$

Fig. 19. Tensile stress-strain model.

$$G_F = G_{F1} + G_{F2} = \int_0^{w_0} \sigma_{ct}(w) d_w + \int_{w_0}^{w_{max}} \sigma_{ct}(w) d_w \tag{17}$$

The tensile stress-crack opening relation at the exponential softening stage was further simplified into bi-linear model which is characterized by the inflection point E (w_1, $\sigma_{ct,w1}$), as shown in Fig. 17(c).

According to Kooiman's [27] study on the tensile post-cracking model of steel fiber reinforced concrete, the ratio of the tensile stress at the inflection point to the tensile strength at the starting point of the exponential softening branch is in between 0.2 and 0.3. In the present study, the tensile stress $\sigma_{ct,w1}$ at the inflection point is taken as $0.2f_{ctr}$. Based on the equal fracture energy G_{F2} for the localized cracking, no matter whether the softening function is in the exponential form or the bi-linear form, i.e., the area enclosed by the three points B, C, and D in Fig. 17(b) is equal to the area enclosed by the four points B, E, C, and D in Fig. 17(c), the cracking opening w_1 is obtained and listed in Table 8. Therefore, the simplified tri-linear model for the tensile stress-crack opening relation is derived below.

$$\begin{cases} \sigma_{ct} = f_{ct} + \dfrac{f_{ctr} - f_{ct}}{w_0} \cdot w & 0 < w \leq w_0 \\[2mm] \sigma_{ct} = f_{ctr} + \dfrac{0.2f_{ctr} - f_{ctr}}{w_1 - w_0} (w - w_0) & w_0 < w \leq w_1 \\[2mm] \sigma_{ct} = 0.2f_{ctr} - \dfrac{0.2f_{ctr}}{w_{max} - w_1} (w - w_1) & w_1 < w \leq w_{max} \end{cases} \tag{18}$$
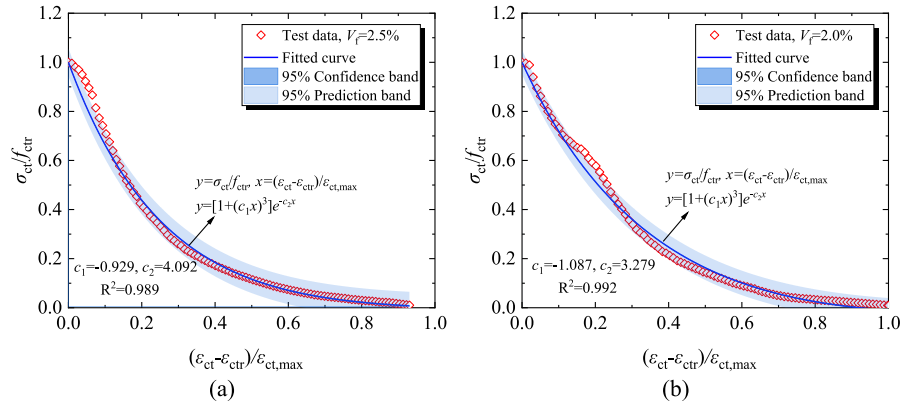
Fig. 20. The fitted tensile stress-strain relation at the exponential softening stage: (a) $V_f = 2.5\%$; (b) $V_f = 2.0\%$.
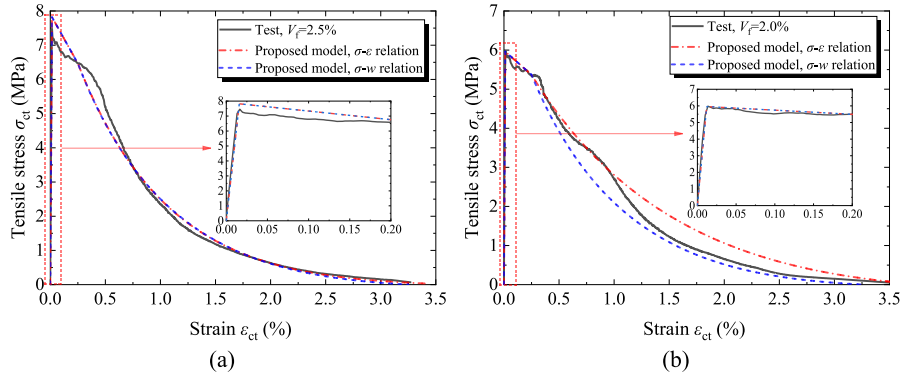

Fig. 21. Comparison of the tensile stress-strain relation of test and proposed models: (a) $V_f = 2.5\%$; (b) $V_f = 2.0\%$.

4.2. Tensile stress-strain model

Based on the monotonic test results, Fig. 19 illustrates the tensile constitutive model of CA-UHPC expressed in terms of strain. The tensile stress-strain relation at the elastic stage is expressed in Eq. (11) aforementioned. At the linear softening stage, the tensile stress-strain relation is described as,

$$\sigma_{ct} = f_{ct} + \frac{f_{ctr} - f_{ct}}{\varepsilon_{ctr} - \varepsilon_{cte}} \cdot (\varepsilon_{ct} - \varepsilon_{cte}) \quad \varepsilon_{cte} < \varepsilon_{ct} \le \varepsilon_{ctr} \tag{19}$$

where ε_{ctr} is the tensile strain at the end point of the linear softening stage and is taken as 0.0025 (corresponding to elongation of 0.5 mm), as summarized in Tables 4 and 5.

The tensile stress-strain relation at the exponential softening stage is fitted in the form of exponential function, as expressed in Eq. (20).

$$\frac{\sigma_{ct}}{f_{ctr}} = \left[1 + c_1 \left(\frac{\varepsilon_{ct} - \varepsilon_{ctr}}{\varepsilon_{ct,max}} \right)^3 \right] e^{-c_2 \frac{\varepsilon_{ct} - \varepsilon_{ctr}}{\varepsilon_{ct,max}}} \quad \varepsilon_{ctr} < \varepsilon_{ct} \le \varepsilon_{ct,max} \tag{20}$$

where $\varepsilon_{ct,max}$ is the maximum tensile stress and is taken as 0.0325 (corresponding to elongation of 6.5 mm), c_1 and c_2 are unknown parameters to be fitted.

Fig. 20 shows the fitted results which exhibit high reliability for the R-square is close to 0.99. The fitted c_1 and c_2 are -0.929 and 4.092 for CA-UHPC with a fiber volume fraction of 2.5% respectively, and are -1.087 and 3.279 for CA-UHPC with a fiber volume fraction of 2.0% respectively.

The tensile stress-crack opening model is converted to the stress-strain relation based on Eq. (13). The comparison of the tensile stress-strain relation of test and two proposed models is plotted in Fig. 21. As shown, the three curves are close to each other and rather narrow.

The two established models agree well with the test results.

5. Numerical verification

5.1. Monotonic uniaxial tensile test

5.1.1. Modelling scheme

Based on the test results of the uniaxial tensile test and four-point bending test for CA-UHPC, finite element analysis (FEA) was conducted using ABAQUS to verify the applicability of the proposed tensile constitutive model for CA-UHPC. In finite element (FE) modelling of concrete structures under tension, the tensile stress-crack opening relation is usually applied in the non-reinforced and less-rebar reinforced concrete structures, while the tensile stress-strain relation is suitable for reinforced concrete structures. Hence, the proposed tensile stress-crack opening relation was adopted in the FEA for CA-UHPC members.

As shown in Fig. 22, a quarter finite element model (FEM) of the dog-bone-shaped specimen under direct tension was established. The FEM was simulated using the eight-node reduced integration element C3D8R. Two symmetric planes, the X surface, and the Z surface, were imposed by the symmetric constraints. To simulate the boundary conditions in the experimental condition accurately, all six degrees of freedom (DOFs) of the FEM lower end were restricted, and the DOFs, U_x, U_z, R_x, R_y, and R_z of the FEM upper end were restricted. The displacement loading was enforced to a reference point which was coupled with the top surface of the FEM.

Fig. 23 shows the concrete damaged-plasticity (CDP) model of ABAQUS. The CDP model is capable of describing damage initiation and accumulation in tension and compression, and failure of tensile cracking and compressive crushing of concrete material. In this study, the CDP
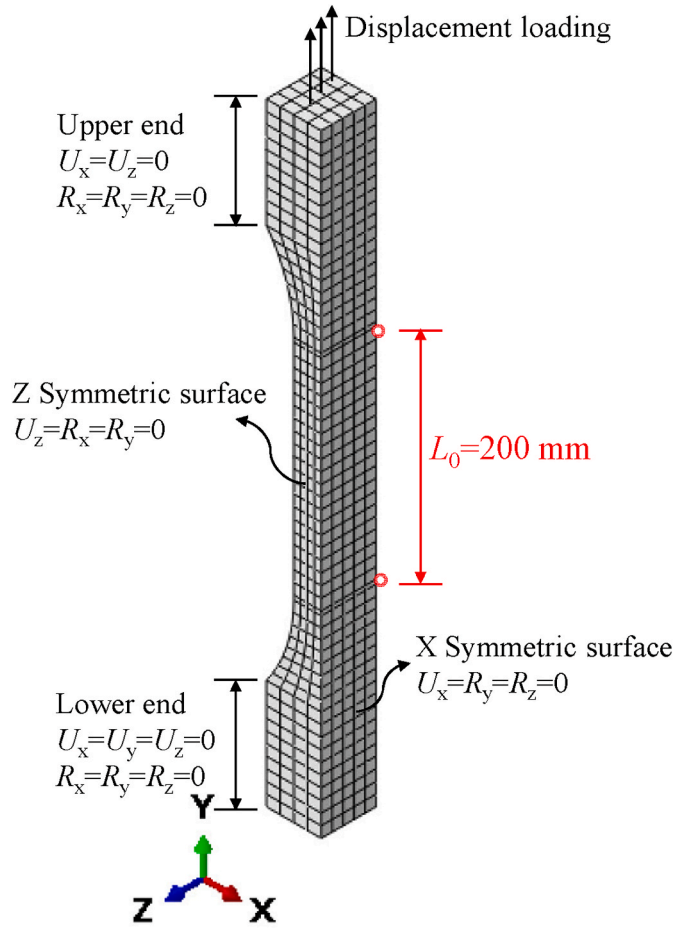
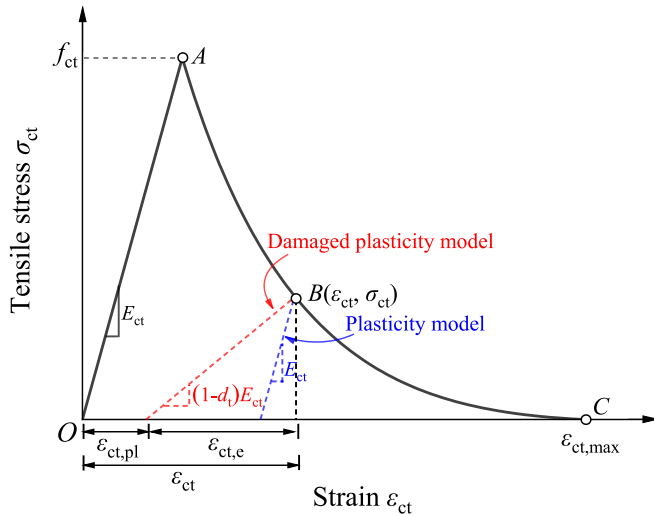**Fig. 22.** Finite element model of direct tensile test.

Fig. 23. CDP model in ABAQUS.

model was used to simulate the plastic behavior and tensile damage evolution of CA-UHPC members under tension. The input plasticity parameters of the CDP model for the CA-UHPC FEM refer to existing research [20], and are listed in Table 9. As illustrated in Fig. 23, the input tensile damage parameter d_t influences the value of the equivalent plastic strain $\varepsilon_{ct,pl}$. In the next paragraph, the influence of d_t on the load-displacement response will be discussed when d_t is considered

Table 9
The plasticity parameters of CDP in ABAQUS.

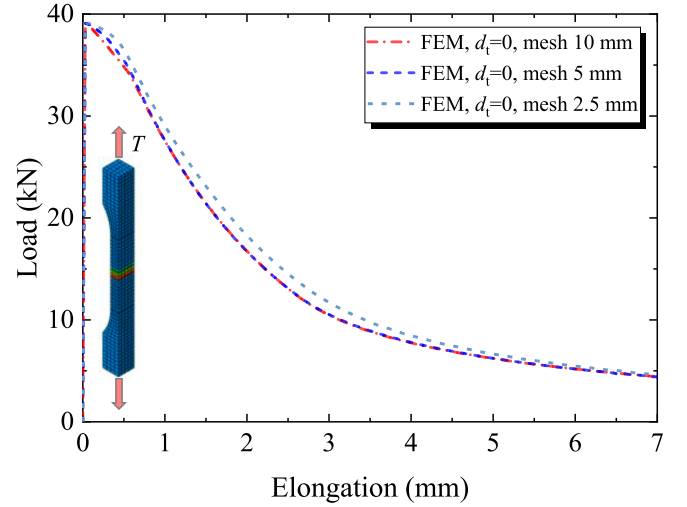| Parameter	Value	Explanation
ψ	54°	Dilation angle
e	0.1	Flow potential eccentricity
f_{b0}/f_{c0}	1.07	The ratio of initial equibiaxial compressive yield stress to initial uniaxial compressive yield stress
k_c	0.666	The coefficient determining the shape of the deviatoric cross-section
μ	0.0001	Viscosity parameter

Fig. 24. The FEM load-elongation curves from different mesh sizes.

under different approaches.

5.1.2. Mesh dependence

Three FE models were generated with mesh sizes of 2.5 mm, 5 mm, and 10 mm to investigate the effect of mesh density on the load-elongation response. In these FE models, the tensile damage parameter d_t was taken as zero. To keep consistent with the uniaxial tensile test, the obtained FEM elongation is the elongation difference of the two end-points within the gauge length of 200 mm, as plotted in Fig. 22. The comparison of the FEM load-elongation curves is shown in Fig. 24. As shown, the influence of the three mesh sizes on the peak load as well as the post-peak response is negligible. To balance the computation efficiency and accuracy, the mesh size of 10 mm was chosen for the following dog-bone FE models.

5.1.3. Comparison of tensile damage variables

Fig. 25 illustrates the comparison of the FEM load-elongation curves, which adopts four different d_t respectively, i.e., $d_t = 0$, $d_t = D_{t,SEP}$, $d_t = D_{t,EEP}$, and $d_t = d_{t,appr}$, and the tested load-elongation curve. In the absence of cyclic tensile test data, the tensile damage variable for concrete is usually approximated as the reduction of the tensile stress at the tensile-softening branch to the tensile strength, as expressed in Eq. (21). The approximated $d_{t,appr}$ has been successfully used in the nonlinear finite element analysis of UHPC beams [28] and slabs [29].

$$d_{t,appr} = 1 - \frac{\sigma_{ct}}{f_{ct}} \tag{21}$$

As compared in Fig. 25, on one hand, the FEM load-elongation curve using $d_{t,appr}$ is in the best agreement with the test result regarding the peak load as well as the tensile-softening response. It indicates that the proposed tensile stress-crack opening model for CA-UHPC can accurately predict the structural response of CA-UHPC member under monotonic uniaxial tension. On the other hand, adopting different
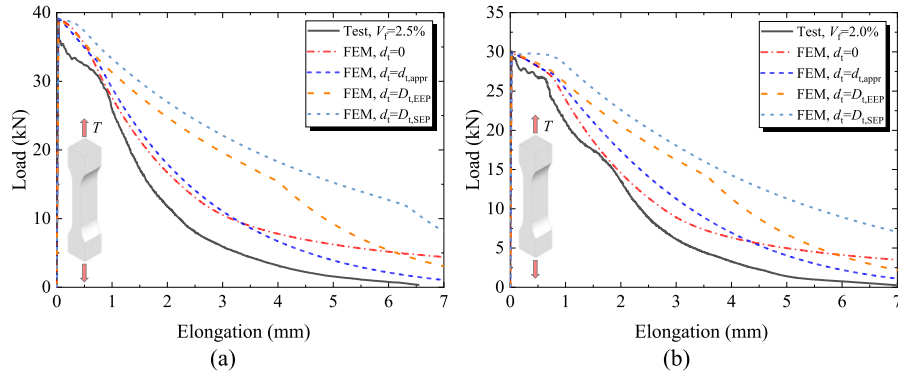
Fig. 25. Comparison of load-elongation curves of test and FEM with different d_t: (a) $V_f = 2.5\%$; (b) $V_f = 2.0\%$.
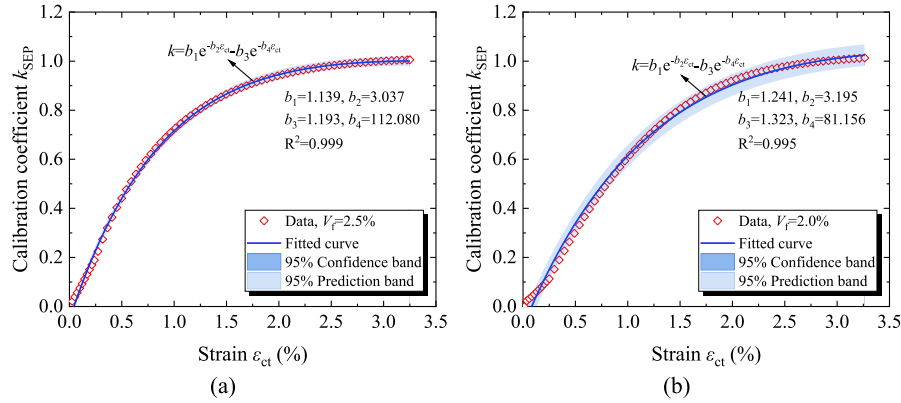

Fig. 26. Calibration coefficient-strain relation for tensile damage variable $D_{t,SEP}$: (a) $V_f = 2.5\%$; (b) $V_f = 2.0\%$.
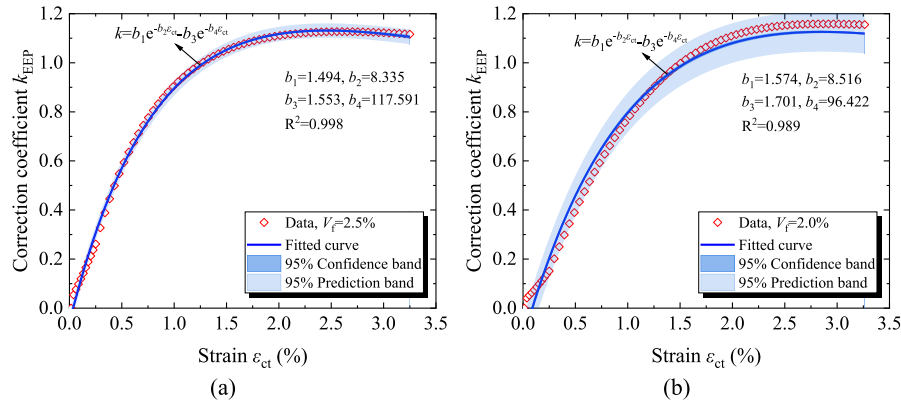

Fig. 27. Calibration coefficient-strain relation for tensile damage variable $D_{t,EEP}$: (a) $V_f = 2.5\%$; (b) $V_f = 2.0\%$.

tensile damage variables induces large differences in the FEM load-elongation response at the softening stage. The FEM using d_t equal to zero yields a good prediction of the load-elongation response when elongation ranges from zero to approximate 4 mm, but overestimates the load-carrying capacity when elongation ranges from approximately 4 mm to 6.5 mm. The two FE models adopting $D_{t,SEP}$ and $D_{t,EEP}$ respectively exhibit poor prediction of the load-elongation response at the softening stage. Therefore, it can be concluded that the tensile damage variables based on the SEP and the EEP cannot be directly taken as the input parameters of CDP in ABAQUS.

Considering the approximated tensile damage variable has the best accuracy to predict the structural response, the tensile damage variables $D_{t,SEP}$, and $D_{t,EEP}$ were calibrated regarding the approximated tensile

Table 10
Fitted parameters of the calibration coefficient-strain relation.

Calibration coefficient	Number	b_1	b_2	b_3	b_4
k_{SEP}	U-2.5%	1.139	3.037	1.193	112.080
	U-2.0%	1.241	3.195	1.323	81.156
k_{EEP}	U-2.5%	1.494	8.335	1.553	117.591
	U-2.0%	1.574	8.516	1.701	96.422

damage variable $d_{t,appr}$. The calibration coefficients k were shown in Eq. (22). The calibration coefficient-strain relation was fitted using the exponential function expressed in Eq. (23). The fitted results were shown in Fig. 26, Fig. 27, and listed in Table 10. Consequently, the
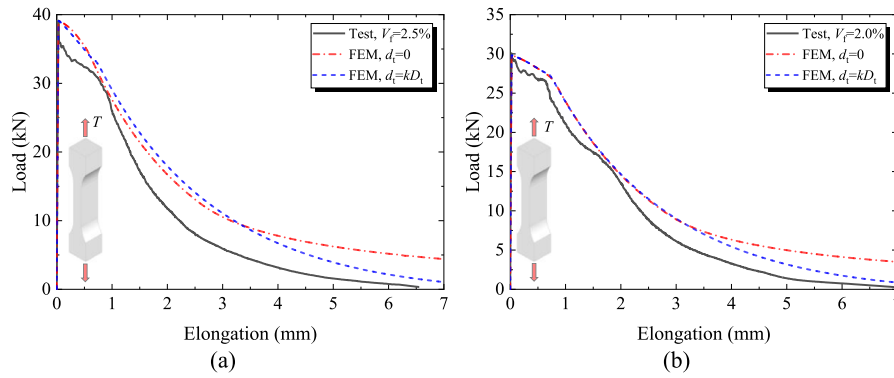
Fig. 28. Comparison of load-elongation curves of test and FEM with calibrated tensile damage variable: (a) V_f = 2.5%; (b) V_f = 2.0%.

calibrated tensile damage variable is derived in Eq. (24).

$$k = \frac{d_{t,appr}}{D_t}$$

$$k_{SEP} = \frac{d_{t,appr}}{D_{t,SEP}} \tag{22}$$

$$k_{EEP} = \frac{d_{t,appr}}{D_{t,EEP}}$$

$$k = b_1 e^{-b_2 \varepsilon_{ct}} - b_3 e^{-b_4 \varepsilon_{ct}} \tag{23}$$

where b_1, b_2, b_3, and b_4 are unknown parameters to be fitted.

$$d_t = kD_t \tag{24}$$

where D_t is shown in Eq. (6), k is shown in Eq. (23).

Fig. 28 compares the load-elongation curves of the test and the FEM using the calibrated tensile damage variable. It is evident that the FEM curve agrees well with the measured curve. This demonstrates that the proposed tensile stress-crack opening model with the cooperation of the calibrated tensile damage variable could provide an accurate prediction of the structural response for CA-UHPC member under monotonic direct tension.

In CDP of ABAQUS, it is assumed that cracking initiates at a point when the tensile equivalent plastic strain is greater than zero, and the maximum principal plastic strain is positive [17]. In addition, the direction of cracking is assumed to be orthogonal to that of the maximum principal plastic strain at the damage point. The FEM-based tensile damage distribution, the FEM-based maximum principal plastic strain, and the tested cracking pattern of the post-peak characterized points are illustrated in Fig. 29. The tensile damage and the maximum principal plastic strain mainly localize at the middle section within the gauge length, which correlate well with the tested localized cracking.

5.2. Cyclic uniaxial tensile test

The dog-bone-shaped specimen under cyclic uniaxial tension was also simulated by FEM using the proposed tensile stress-crack opening model and the calibrated tensile damage variable. To make comparison, the experimental elongation values of loading-unloading cycles were used as input data in FEM. Fig. 30 compares the tested and the FEM-based load-elongation responses. In general, the FEM results shows good agreement with the test results. It indicates that the proposed tensile stress-crack opening model with the cooperation of the calibrated tensile damage variable also could provide an effective prediction of the structural response for CA-UHPC member under cyclic direct tension.

5.3. Four-point bending test

Four-point bending test (4 PT) of CA-UHPC was conducted to investigate the flexural behavior. The specimen geometry of the 4 PT is shown in Fig. 31. To validate the applicability of the proposed tensile constitutive model in the analysis of the flexural behavior of CA-UHPC member, the FEM of 4 PT was established and the obtained load-displacement curve was compared with the test curve.

Fig. 32 shows the FEM of the CA-UHPC beam under four-point bending. A half model in the X direction was established. The FEM was simulated using the eight-node reduced integration element C3D8R. The symmetric X surface was imposed by the symmetric constraints where the DOFs of Ux, Ry, and Rz were restricted. The simply supported constraint boundary was simulated by restricting the DOFs of Ux, Uy, Ry, and Rz of the bearings. The displacement loading was enforced to a reference point coupled with the top surfaces of the loading beams.
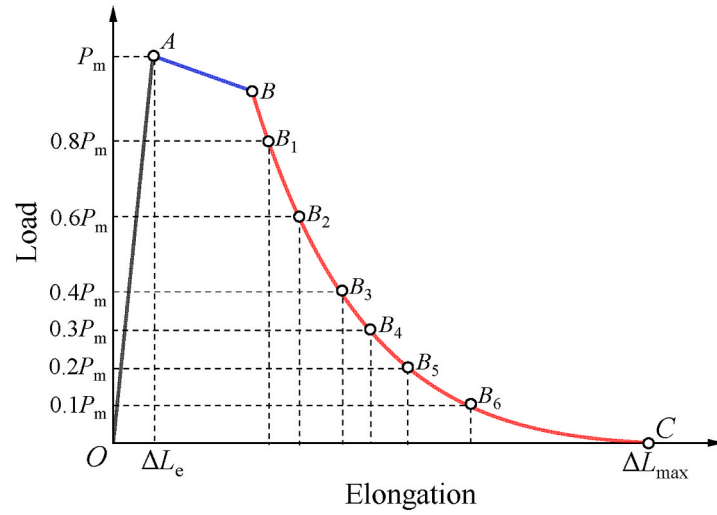
As plotted in Fig. 33, mesh sizes of 5 mm, 10 mm, and 20 mm were compared to study the effect of mesh density on the load-midspan deflection response. The tensile damage parameter d_t was taken as zero in the three FE models. It is evident that the mesh size of 20 mm exerts a relatively large deviation of the post-peak load-midspan deflection response compared with the mesh size of 10 mm and 5 mm. Considering that the mesh sizes of 10 mm and 5 mm provide a slight difference at the peak load as well as the post-peak response, the mesh size of 10 mm was taken to simulate the CA-UHPC beam in the subsequent FE models.

Fig. 34 compares the load-midspan deflection responses of the test and the FEM. The peak loads obtained by FE models using the two different tensile damage variables are almost equal to the test result. Regarding the post-peak response, the FEM using the calibrated tensile damage variable provides better agreement with the test result. But with regard to the mid-span deflection corresponding to the peak load, the FEM value is approximately half of the test value. This could be interpreted by the different cracking patterns of the test and the FEM, as illustrated in Fig. 35.

The localized cracking could initiate and propagate at any section of the pure bending zone in the four-point bending test, such as the mid-span section, and the loading-point section. In the FEM, two symmetric localized cracks are obtained at the loading-point sections. The simulated beam is more likely to be split into three components by the two symmetric localized cracks. In this situation, the deflection value of the mid-span section is identical to that of the loading-point section in FEM. Therefore, the FEM-based mid-span deflection corresponding to the peak load is smaller than the test result. All in all, considering the whole load-midspan deflection response, the proposed tensile stress-crack opening model with the cooperation of the calibrated tensile damage variable could effectively simulate the flexural behavior of CA-UHPC member.

6. Conclusions

Based on the above investigations, the main conclusions are:
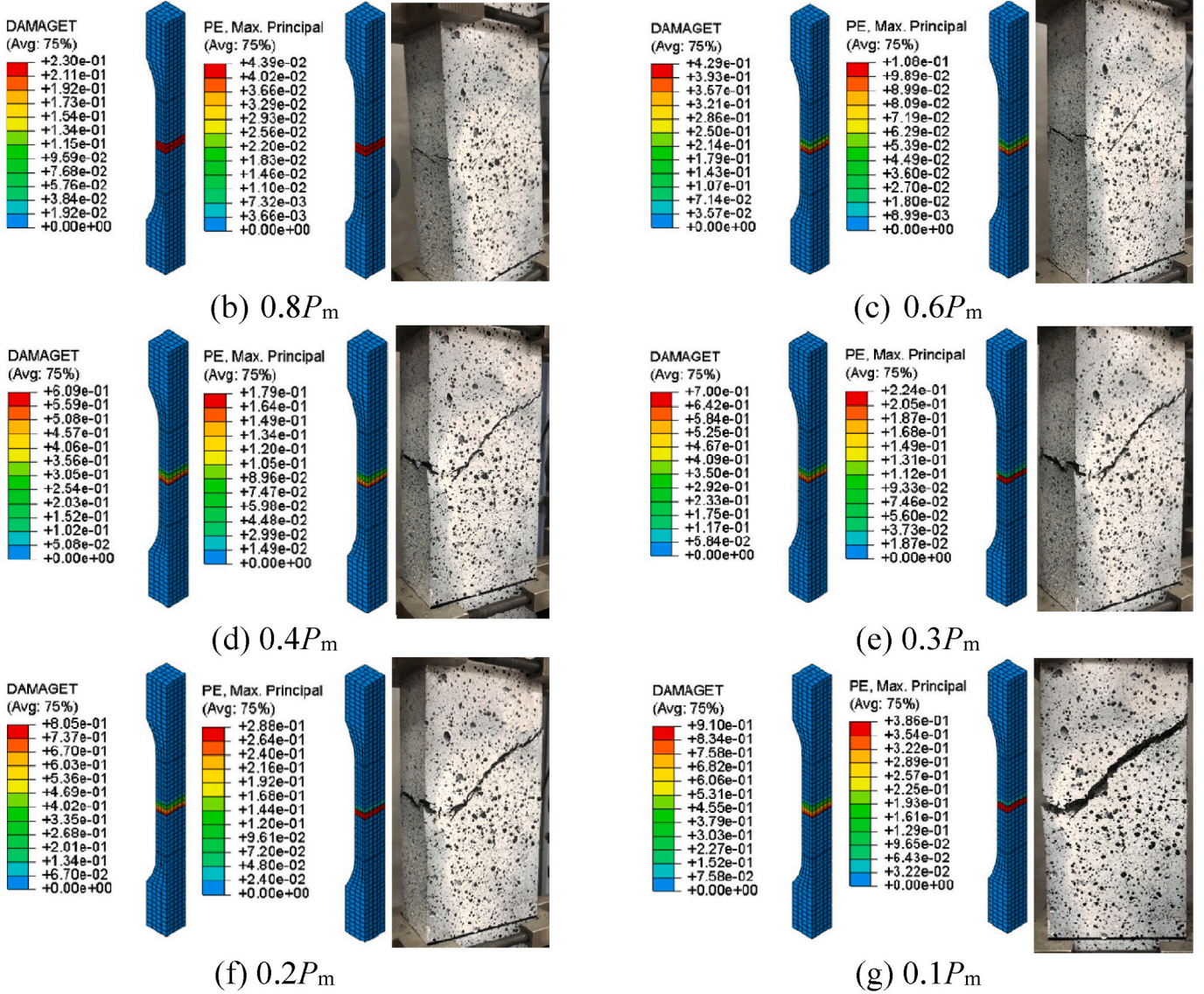
(a) The post-peak characterized points.

(b) $0.8P_\mathrm{m}$

(c) $0.6P_\mathrm{m}$

(d) $0.4P_\mathrm{m}$

(e) $0.3P_\mathrm{m}$

(f) $0.2P_\mathrm{m}$

(g) $0.1P_\mathrm{m}$

Fig. 29. The tensile damage distribution and cracking pattern of dog-bone-shaped specimen (CA-UHPC with a fiber volume fraction of 2.5%).

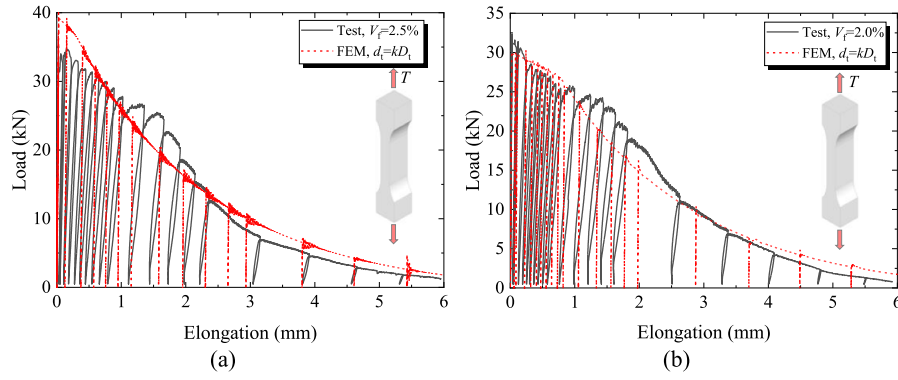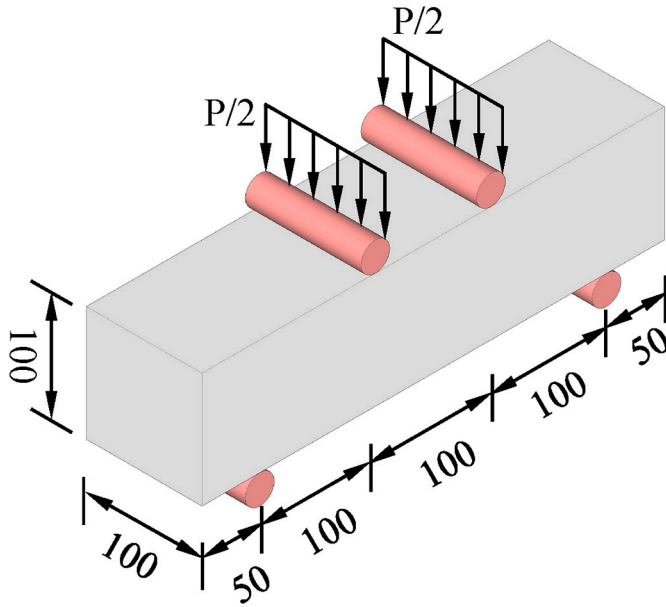**Fig. 30.** Comparison of cyclic load-elongation curves of test and FEM: (a) $V_f = 2.5\%$; (b) $V_f = 2.0\%$.

Fig. 31. Four-point bending test of CA-UHPC (unit: mm).

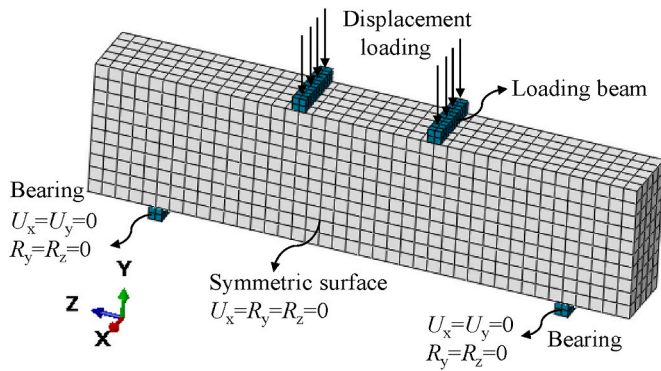**Fig. 33.** The FEM load-elongation curves from different mesh sizes.

Fig. 32. Finite element model of four-point bending test.

(1) The CA-UHPC with steel fiber volume fractions of 2.5% and 2.0% exhibits linear stress-strain relation up to the tensile strength, and tensile softening response featured by the smeared- and localized-cracking stages.

(2) Considering the elastic stage as well as the tensile-softening stage, the envelope tensile stress-strain curve of CA-UHPC under cyclic uniaxial tension is approximately 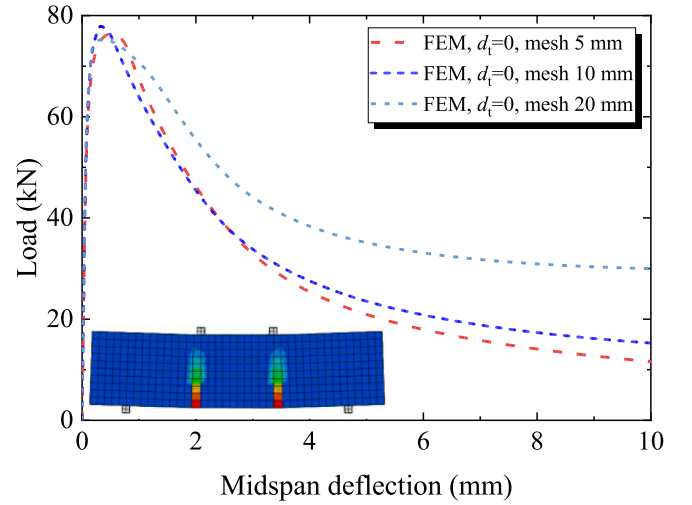aligned with the tensile stress-strain curve under monotonic uniaxial tension. The monotonic tensile stress-strain curve could be adopted to predict the cyclic tensile envelope curve.

(3) The fracture energy of CA-UHPC could be decomposed into two components, one for smeared cracking and the other one for localized cracking. The fracture energy of CA-UHPC with a fiber volume fraction of 2.5% is 2.15 N/mm for smeared cracking, and 10.21 N/mm for localized cracking. The fracture energy of CA-UHPC with a fiber volume fraction of 2.0% is 1.70 N/mm for smeared cracking, and 9.71 N/mm for localized cracking.

(4) Based on the cyclic tensile test results, the established tensile damage evolution laws according to the strain equivalence principle and the energy equivalence principle respectively, cannot be directly used as the input tensile damage parameter in CDP.

(5) The proposed tensile stress-crack opening model with the cooperation of the calibrated tensile damage variable could provide an effective prediction of the structural response for CA-UHPC members under monotonic tension as well as under cyclic tension.

Declaration of competing interest

The authors declare that they have no known competing financial interests or personal relationships that could have appeared to influence the work reported in this paper.
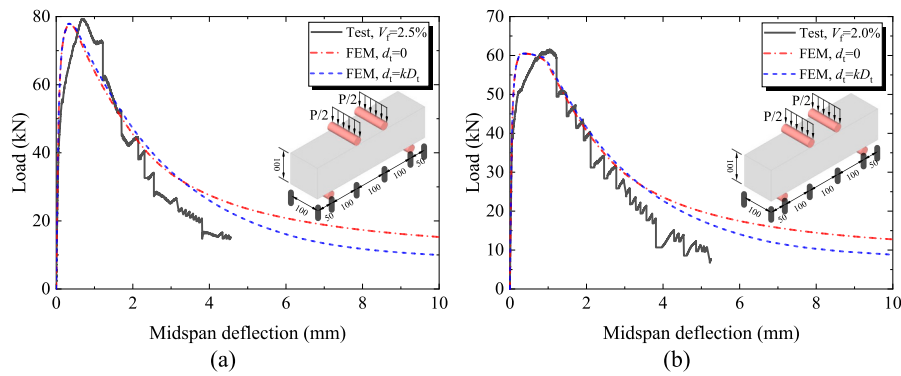
Fig. 34. Comparison of load-midspan deflection curves of test and FEM: (a) $V_f = 2.5\%$; (b) $V_f = 2.0\%$.

(a) Cracking pattern

(b) Tensile damage

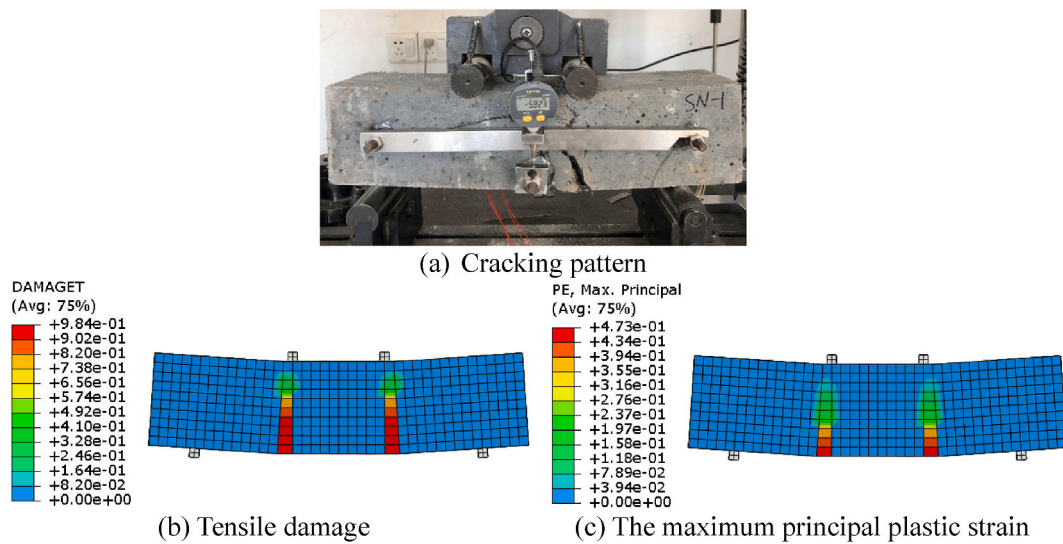(c) The maximum principal plastic strain

Fig. 35. Cracking pattern and tensile damage distribution of CA-UHPC beam with fiber volume fraction of 2.5% at the post-peak load-carrying capacity of 15 kN.

Data availability

Data will be made available on request.

References

[1] Z.B. Haber, I.D. la Varga, B.A. Graybeal, B. Nakashoji, R. El-Helou, Properties and Behavior of UHPC-Class Materials, Fhwa-Hrt-18-036, 2018, p. 153.

[2] MCS-EPFL, Ultra-High Performance Fibre Reinforced Cement-based composites (UHPFRC) Construction material , dimensioning und application, 2016.

[3] Association Francaise de Normalisation, Concrete-ultra-high Performance Fibre-Reinforced Concrete-Specifications, Performance, Production and Conformity, 2016. NF P.

[4] C. Tasdemir, M.A. Tasdemir, F.D. Lydon, B.I.G. Barr, Effects of silica fume and aggregate size on the brittleness of concrete, Cement Concr. Res. 26 (1996) 63–68, https://doi.org/10.1016/0008-8846(95)00180-8.

[5] S. Pyo, H.K. Kim, B.Y. Lee, Effects of coarser fine aggregate on tensile properties of ultra high performance concrete, Cem. Concr. Compos. 84 (2017) 28–35, https://doi.org/10.1016/j.cemconcomp.2017.08.014.

[6] X. Zeng, K. Deng, H. Liang, R. Xu, C. Zhao, B. Cui, Uniaxial behavior and constitutive model of reinforcement confined coarse aggregate UHPC, Eng. Struct. 207 (2020), 110261, https://doi.org/10.1016/j.engstruct.2020.110261.

[7] J. Ma, M. Orgass, F. Dehn, D. Schmidt, N.V. Tue, Comparative investigations on ultra-high performance concrete with or without coarse aggregates, Proc. Int. Symp. Ultra High Perform. Concr. Kassel. (2004) 205–212.

[8] A. Cwirzen, V. Penttala, C. Vornanen, Reactive powder based concretes: mechanical properties, durability and hybrid use with OPC, Cement Concr. Res. 38 (2008) 1217–1226, https://doi.org/10.1016/j.cemconres.2008.03.013.

[9] K. Wille, C. Boisvert-Cotulio, Material efficiency in the design of ultra-high performance concrete, Construct. Build. Mater. 86 (2015) 33–43, https://doi.org/10.1016/j.conbuildmat.2015.03.087.

[10] D.Y. Yoo, Y.S. Yoon, Structural performance of ultra-high-performance concrete beams with different steel fibers, Eng. Struct. 102 (2015) 409–423, https://doi.org/10.1016/j.engstruct.2015.08.029.

[11] J. Liu, F. Han, G. Cui, Q. Zhang, J. Lv, L. Zhang, Z. Yang, Combined effect of coarse aggregate and fiber on tensile behavior of ultra-high performance concrete, Construct. Build. Mater. 121 (2016) 310–318, https://doi.org/10.1016/j.conbuildmat.2016.05.039.

[12] P.P. Li, Q.L. Yu, H.J.H. Brouwers, Effect of coarse basalt aggregates on the properties of Ultra-high Performance Concrete (UHPC), Construct. Build. Mater. 170 (2018) 649–659, https://doi.org/10.1016/j.conbuildmat.2018.03.109.

[13] Y. Wang, X. Shao, J. Cao, Experimental study on basic performances of reinforced UHPC bridge deck with coarse aggregates, J. Bridge Eng. 24 (2019) 1–11, https://doi.org/10.1061/(asce)be.1943-5592.0001492.

[14] K. Wang, K. Deng, C. Zhao, C. Wang, Experimental investigation of bending behavior of reinforced ultra-high-performance concrete decks, Front. Built Environ. 5 (2019) 1–10, https://doi.org/10.3389/fbuil.2019.00135.

[15] J. Qi, Y. Bao, J. Wang, L. Li, W. Li, Flexural behavior of an innovative dovetail UHPC joint in composite bridges under negative bending moment, Eng. Struct. 200 (2019), 109716, https://doi.org/10.1016/j.engstruct.2019.109716.

[16] H. Hadi, N. Mirshekari, V. Sarfaraziet, M. Fatehimarji, Numerical simulation of compressive to tensile load conversion for determining the tensile strength of ultra-high performance concrete, Smart Structures and Systems, Int. J. 26 (5) (2020) 605–617.

[17] J. Lubliner, J. Oliver, S. Oller, E. Oñate, A plastic-damage model for concrete, Int. J. Solid Struct. 25 (1989) 299–326, https://doi.org/10.1016/0020-7683(89)90050-4.

[18] J. Lee, G.L. Fenves, Plastic-damage model for cyclic loading of concrete structures, J. Eng. Mech. 124 (1998) 892–900, https://doi.org/10.1061/(asce)0733-9399(1998)124:8(892).

[19] S.A. Paschalis, A.P. Lampropoulos, Ultra-high-performance fiber-reinforced concrete under cyclic loading, ACI Mater. J. 113 (2016) 419–427, https://doi.org/10.14359/51688928.

[20] P.A. Krahl, R. Carrazedo, M.K. El Debs, Mechanical damage evolution in UHPFRC: experimental and numerical investigation, Eng. Struct. 170 (2018) 63–77, https://doi.org/10.1016/j.engstruct.2018.05.064.

[21] X. Gao, J. Wang, J. Guo, C. Liu, Axial tensile mechanical properties and constitutive relation model of ultra-high performance concrete under cyclic loading, Acta Mater. Compos. Sin. 38 (2021) 3925–3938.

[22] CECS(China Association for Engineering Construction Standardization), CECS13: 2009, Standard Test Methods for Fiber Reinforced Concrete, China Plan. Press, 2009.

[23] A. Hillerborg, M. Modéer, P.-E. Petersson, Analysis of crack formation and crack growth in concrete by means of fracture mechanics and finite elements, Cement Concr. Res. 6 (1976) 773–782.

[24] J. Lemaitre, How to use damage mechanics, Nucl. Eng. Des. 80 (1984) 233–245.

[25] F. Supartono, F. Sidoroff, Anisotropic damage modeling for brittle elastic materials, Arch. Mech. 37 (1985) 521–534.

[26] D.A. Hordijk, Local Approach to Fatigue of Concrete, Delft University of Technology, 1991.

[27] A.G. Kooiman, C. Van Der Veen, J.C. Walraven, Modelling the post-cracking behaviour of steel fibre reinforced concrete for structural design purposes, Heron 45 (2000) 275–307.

[28] G.H. Mahmud, Z. Yang, A.M.T. Hassan, Experimental and numerical studies of size effects of ultra high performance steel fibre reinforced concrete (UHPFRC) beams, Construct. Build. Mater. 48 (2013) 1027–1034, https://doi.org/10.1016/j.conbuildmat.2013.07.061.

[29] M.M.A. Kadhim, A.R. Saleh, L.S. Cunningham, A.A. Semendary, Numerical investigation of non-shear-reinforced UHPC hybrid flat slabs subject to punching shear, Eng. Struct. 241 (2021), 112444, https://doi.org/10.1016/j.engstruct.2021.112444.